Dense single-atomic $14\times\sqrt{3}$-reconstructed Pb layer on Si(111): Structural and superconducting properties

L. V. Bondarenko,[1] A. Y. Tupchaya,[1] Y. E. Vekovshinin,[1] D. V. Gruznev,[1] Tatiana V. Utas,[1] A. N. Mihalyuk,[1,2] N. V. Denisov,[1] A. V. Zotov,[1] and A. A. Saranin[1]

[1]*Institute of Automation and Control Processes, FEB RAS, 690041 Vladivostok, Russian Federation*

[2]*Institute of High Technologies and Advanced Materials, Far Eastern Federal University, 690950 Vladivostok, Russian Federation*

(Received 23 June 2023; revised 18 August 2023; accepted 5 September 2023; published 19 September 2023)

A highly ordered, Pb-dense $14\times\sqrt{3}$-Pb overlayer was grown on Si(111) using the two-step procedure with formation of the $\sqrt{7}\times\sqrt{3}$-Pb surface [displaying the 1×1 structure at room temperature (RT)] at the first step and RT deposition of additional Pb at the second step until formation of the $14\times\sqrt{3}$-Pb phase with 1.286 monolayers of Pb is completed. The single-domain orientation of the $14\times\sqrt{3}$-Pb layer persists along the entire surface of the terraces which are typically as wide as dozens of nanometers and in the selected areas might exceed a hundred nanometers. The $14\times\sqrt{3}$-Pb phase hosts the superconductivity with the critical temperature $T_c = 2.08$ K which exceeds all ever reported values for the single-atom Pb layers on Si(111).

DOI: 10.1103/PhysRevB.108.115428

I. INTRODUCTION

Among other metal/silicon reconstructions (i.e., ordered atomic-layer metal films grown on single-crystalline silicon substrates), those formed in the Pb/Si(111) system at Pb coverages beyond one monolayer (1.0 ML $= 7.8\times10^{14}$ cm^{-2}) have attracted especial interest due to a number of the possessed fascinating properties and displayed phenomena (e.g., nonvortical spin texture with large energy splitting [1,2], anomalous ultrafast mass transport [3–7], and superconductivity at a single-atom-layer limit [8,9]). Recall that the Pb/Si(111) phase diagram beyond 1.0 ML is rich and complicated [10]. It contains the $\sqrt{7}\times\sqrt{3}$-Pb with 1.20 ML of Pb [11–14], the densest so-called striped incommensurate SIC-Pb phase with 1.28–1.30 ML of Pb (less than 1.33 ML, an ideal coverage of the $\sqrt{3}\times\sqrt{3}$-Pb phase) [10], as well as the so-called hexagonal incommensurate HIC-Pb phase [15] and a set of the "devil's staircase" (DS) phases [16] at the intermediate coverage range comprising the mixed phases of local $\sqrt{7}\times\sqrt{3}$ and $\sqrt{3}\times\sqrt{3}$ atomic structures. The structural alternative to the SIC-Pb phase is the commensurate $14\times\sqrt{3}$-Pb phase which is formed on the vicinal Si(111) surfaces with miscut angle of 2° [17] or 3° [18] (remarkably, the SIC-Pb phase remains at the Si(111) surface with 1.1° miscut [19]).

The single-atom Pb layers on Si(111) have been proved to be a valuable prototype system to explore various aspects of the superconductivity at the ultimate thickness limit, including the remarkable effects of disorder [20], the roles of the atomic steps [19,21–23], the electron-phonon and spin-orbit couplings [24,25], and the Berezinskii-Kosterlitz-Thouless transition [24–26]. As concerns the critical temperature T_c, almost all available data (albeit limited) are for the SIC-Pb phase. The scanning tunneling spectroscopy (STS) measurements by Zhang *et al.* [8] yielded $T_c = 1.83$ K. The transport measurements of various groups yielded various T_c values. In particular, Yamada *et al.* [9] obtained the T_c of 1.1 K. In the measurements by Baranov *et al.* [23], zero resistance on the pristine SIC-Pb sample was not reached even at 1.15 K, but on the SIC-Pb sample with Au-decorated atomic steps the measured T_c equals 1.25 K. In the very recent work by Sato *et al.* [19], the transport measurements yielded T_c of 1.51 K and 1.21 K for the SIC-Pb phase on the flat and 1.1°-tilted vicinal Si(111) substrates, respectively. The data set for the other single-atom Pb layers is still more limited. In the STS measurements by Zhang *et al.* [8], $T_c = 1.52$ K was obtained for the $\sqrt{7}\times\sqrt{3}$-Pb phase. Brun *et al.* [20] detected and explored the superconducting properties of the $\sqrt{7}\times\sqrt{3}$-Pb phase at 0.3 K and Oguro *et al.* [22] explored those of the $\sqrt{3}\times\sqrt{43}$-Pb (1.23 ML of Pb) phase (which is one of the "devil's staircase" phases) at 0.4 K; in the both works the STS technique was employed.

The typical procedure used to prepare the SIC-$\sqrt{3}\times\sqrt{3}$-Pb phase involves room-temperature (RT) deposition of an excess amount (e.g., 1.5–2.0 ML) of Pb onto the Si(111)7×7 surface and subsequent annealing at 350–550 °C to desorb surplus Pb and to form the phase. In the present work, we used an alternative procedure, as follows. First, the $\sqrt{7}\times\sqrt{3}$-Pb surface was prepared using a procedure similar to the above described one differing only by the duration of annealing. [Note that the $\sqrt{7}\times\sqrt{3}$-Pb surface at RT displays in LEED and STM the 1×1 structure, which is ascribed to the melted phase [27,28]. Recall that, besides the SIC-$\sqrt{3}\times\sqrt{3}$-Pb and HIC-$\sqrt{3}\times\sqrt{3}$-Pb phases, the other single-layer phases (i.e., $\sqrt{7}\times\sqrt{3}$-Pb and "devil's staircase" phases) are observed only at low (e.g., liquid-nitrogen) temperatures.] At the second step, an additional Pb was deposited onto the $\sqrt{7}\times\sqrt{3}$-Pb (1×1-Pb) surface at RT sequentially until the Pb-densest phase, which appeared to be the $14\times\sqrt{3}$-Pb phase with 1.286 ML of Pb, covered the entire surface. The $14\times\sqrt{3}$-Pb phase has a

single-domain structure of exceptionally high crystalline quality. The proposed procedure not only produces the high-quality dense Pb layer, but also can be a useful tool to scan the narrow Pb coverage range from 1.20 ML to 1.29 ML in a step-by-step manner using sequential deposition of the desired amount of Pb at each step. In particular, we employed this possibility in order to explore the evolution of the transport (superconducting) properties of the Pb/Si(111) system with monotonically growing Pb coverage in this range. In particular, it has been found that the critical temperature T_c grows gradually with Pb coverage and for the Pb-densest $14\times\sqrt{3}$-Pb phase T_c equals 2.08 K, which exceeds all ever reported values for the single-atom Pb layers on Si(111).

II. EXPERIMENTAL AND CALCULATION METHODS

Experiments were performed in the two separate ultrahigh-vacuum (UHV) systems depending on the research tasks. In particular, characterization of the growth mode, as well as the structural and electronic properties of the Pb/Si(111) samples, was conducted in the UHV Omicron MULTIPROBE system equipped with scanning tunneling microscopy (STM), low-energy electron diffraction (LEED), and angle-resolved photoelectron spectroscopy (ARPES) facilities. The electron transport measurements of the samples at low temperatures were performed in the UNISOKU USM 1500 LT STM system, equipped with a superconducting magnet and the four-point-probe (4PP) technique. The base pressure in the both UHV systems was on the order of 1×10^{-10} Torr. To prepare the atomically clean Si(111)7×7 surfaces, the Si(111) samples were first annealed *in situ* at 600 °C for several hours and finally were flashed to 1280 °C. Pb was deposited from a Ta tube. STM images were acquired in a constant-current mode with a mechanically cut PtIr tip after annealing in vacuum. ARPES measurements were conducted using a VG Scienta R3000 electron analyzer and high-flux He discharge lamp with a toroidal-grating monochromator as a light source. The 4PP head mount on the STM stage instead of the tip holder was used for the *in situ* transport measurements. Gold wires of 0.1 mm in diameter equally spaced by 0.2 mm along the straight line were used for the probes. Low temperatures were calibrated in the special experiments with the additional temperature sensor directly attached to the sample and using the samples with thick films of materials with known superconductivity critical temperatures.

We performed the density functional theory (DFT) calculations using the Vienna *ab initio* simulation package [29,30], with core electrons represented by projector augmented wave potentials [30,31]. The generalized gradient approximation (GGA) of Perdew, Burke, and Ernzerhof (PBE) [32] was used as the exchange-correlation functional. To simulate the Pb/Si(111)-$14\times\sqrt{3}$ surface we used a slab consisting of 4 bilayers (BLs) of the substrate with optimized bulk Si lattice constant. Hydrogen atoms were used to passivate the Si dangling bonds. The positions of surface atoms and atoms of Si layers within two BLs were optimized until the residual forces on atoms became smaller than 10 meV/Å. The scalar relativistic effects and the spin-orbit coupling were included in the calculation of band structures. The $1\times7\times1$, k-point mesh was used to sample the $14\times\sqrt{3}$ surface Brillouin zone (SBZ). The unfolding of the band structure was made using the BandUP code [33,34].

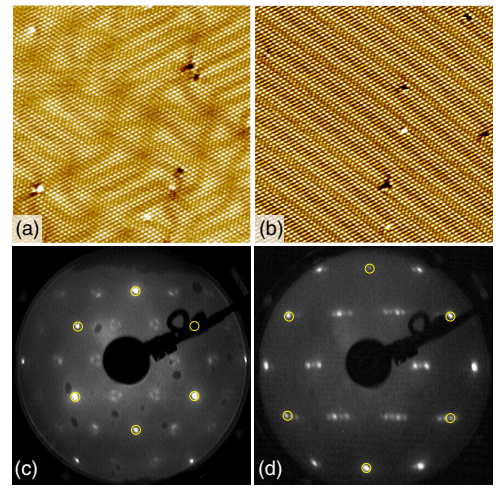

FIG. 1. STM images (400×400 Å^2) and LEED patterns of the densest single-atom Pb layers formed on the Si(111) surface upon growth using alternative formation procedures: (a), (c) SIC-Pb phase and (b), (d) $14\times\sqrt{3}$-Pb phase. The main reflections in the LEED patterns are outlined by yellow circles. LEED electron beam energies are (c) 75 eV and (d) 38 eV.

III. RESULTS

Figure 1 illustrates the structural difference between the densest Pb atomic layers on Si(111) prepared using the conventional formation procedure [Figs. 1(a) and 1(c)] and the procedure proposed in the present study [Figs. 1(b) and 1(d)]. The former is the well-known SIC-Pb phase formed by RT deposition of Pb onto the bare Si(111)7×7 surface followed by annealing. The SIC phase displays in the STM a triple-domain structure with meandering domain walls [Fig. 1(a)]. In the LEED patterns [Fig. 1(c)], the triple-domain structure is known to be reflected by occurrence of three smeared lobelike spots around the nominal position of the $\sqrt{3}$ reflection [10]. The most essential peculiarity of the alternative procedure is the RT deposition of Pb onto the $\sqrt{7}\times\sqrt{3}$-Pb (which looks up as 1×1 at RT) at the final stage, which results overall in the formation of the single-domain $14\times\sqrt{3}$-Pb phase, as evidenced in STM and LEED observations [Figs. 1(b) and 1(d), respectively]. Possible variation of the procedure resides in preparation at the first step of the $\sqrt{3}\times\sqrt{3}$-Pb (1/3 ML of Pb) surface instead of the $\sqrt{7}\times\sqrt{3}$-Pb one. The shortage of this procedure is associated with the presence of Si adatoms incorporated in the $\sqrt{3}\times\sqrt{3}$-Pb reconstruction [35,36]. At the second step, these Si atoms agglomerate into the seldom Si atomic wires, similar to those observed at Si deposition onto the Pb-monolayer-covered Si(111) surface [37]. In all other respects, the formed $14\times\sqrt{3}$-Pb surfaces are essentially identical. The $14\times\sqrt{3}$-Pb layer uniformly covers the entire sample surface, it is free of domain walls, and its single-domain orientation is set along the direction perpendicular to the $[1\bar{1}0]$ atomic steps of the Si(111) substrates (see Fig. S1 of the Supplemental Material [44]). Note that the behavior is similar to the formation of $14\times\sqrt{3}$-Pb structure on the

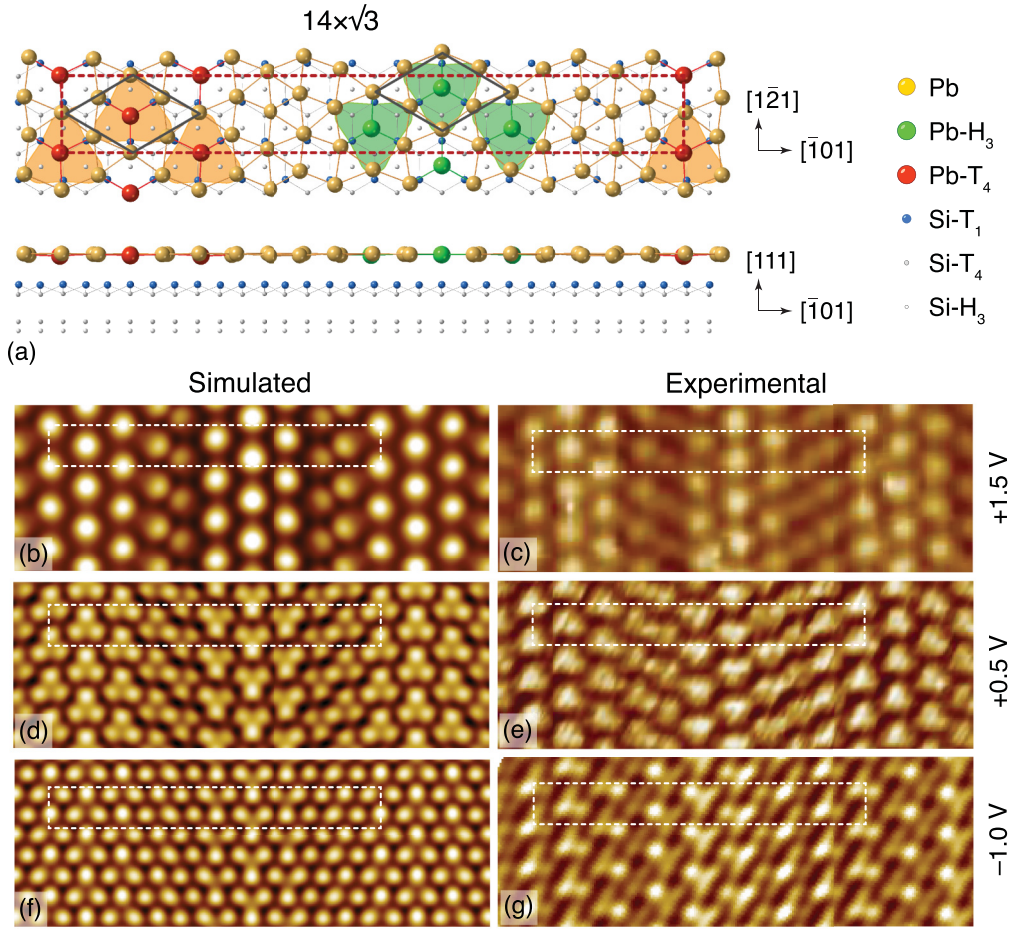

FIG. 2. (a) Ball-and-stick structural model of the $14\times\sqrt{3}$-Pb phase (top and side views). The Pb atoms residing in the regular T_4 positions are shown by red balls, those in the regular H_3 positions by green balls, the other Pb atoms in various nonregular positions by yellow balls. Si atoms in the on-top (T_1), T_4, and H_3 sites shown by blue, gray, and white balls, respectively. The triangles around Pb atoms in the T_4 and H_3 sites are hatched in orange and light green, respectively, to guide the eye. The rectangular $14\times\sqrt{3}$ unit cell is outlined by a red dashed rectangle. The black $\sqrt{3}\times\sqrt{3}$ rhombuses mark the region where atomic arrangement of Pb atoms almost reproduces the ideal $\sqrt{3}\times\sqrt{3}$-Pb phase. A set of three panels shows pairs of the simulated and experimental high-resolution STM images obtained at (b), (c) +1.5 V, (d), (e) +0.5 V, and (f), (g) −1.0 V sample bias voltages. The $14\times\sqrt{3}$ unit cells are outlined by the white dashed rectangles.

vicinal 2°-miscut Si(111) samples [17], but there is an essential difference in the terrace width, which is nominally ∼6.0 nm in those vicinal samples, while in the present case the terraces are as wide as several dozen nanometers and in the selected areas exceed a hundred nanometers. The atomic structure of the $14\times\sqrt{3}$-Pb phase was disclosed using comprehensive analysis of the high-resolution STM images (see Fig. 2S of the Supplemental Material [44]) combined with the results of the DFT calculations. The ball-and-stick model of the resultant structure is presented in Fig. 2(a). The structure adopts 28 Pb atoms per $14\times\sqrt{3}$ unit cell, which corresponds to the 1.286 ML Pb coverage. One can see that the atomic arrangement of the $14\times\sqrt{3}$-Pb phase can be visualized as consisting of alternating rows in which Pb atoms occupy either the H_3 sites and close to them [these atoms are shown by green balls in Fig. 2(a)] or the T_4 sites and close to those (shown by red balls); the other Pb atoms (shown by yellow balls) occupy various nonregular sites and constitute the transient areas between the Pb (H_3) and Pb (T_4) rows. The Pb layer is atomically flat with the height difference of Pb atoms being less than ∼0.02 nm. Simulated STM images demonstrate a fairly good consistency with the experimental ones, including the fine features. In particular, one can see that at +0.5 V bias voltage [Figs. 2(d) and 2(e)] Pb atoms show up as "trimers" having opposite orientations in the Pb (H_3) and Pb (T_4) rows, the corresponding counterparts in the model [Fig. 2(a)] being indicated by the triangles hatched in green and red. One can argue that consistency of STM images at −1.0 V bias voltage is not so apparent. However, close inspection reveals that each characteristic feature (i.e., separate protrusions, sometimes being arranged in the trimers) in the simulated image has a direct counterpart in the experimental one and vice versa. All experimental features are slightly smeared in the diagonal direction, which can be attributed to the asymmetric shape of the STM tip. It is worth noting that alternative structural models, namely the $14\times\sqrt{3}$-Pb structure built according to the "devil's staircase" model with six $\sqrt{3}\times\sqrt{3}$ unit cells separated by two $\sqrt{7}\times\sqrt{3}$ units [17] and $13\times\sqrt{3}$-Pb structure [2], were also examined and were found to be strongly energetically unfavorable, compared to the present model, and their simulated

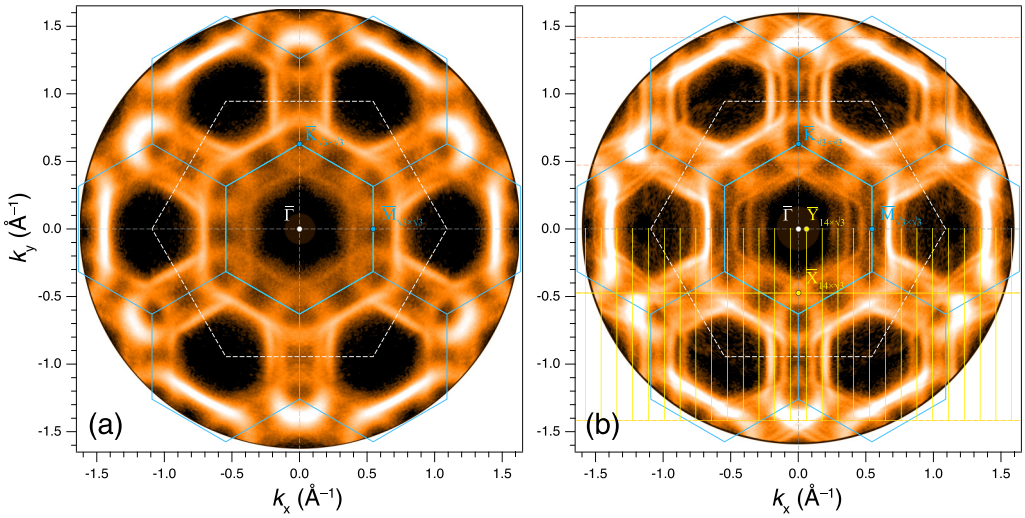

FIG. 3. ARPES Fermi maps from (a) SIC-Pb and (b) $14\times\sqrt{3}$-Pb surfaces. The surface Brillouin zones (SBZs) for the 1×1, $\sqrt{3}\times\sqrt{3}$, and $14\times\sqrt{3}$ periodic structures are outlined with white, blue, and yellow lines, respectively. The high-symmetry points in the corresponding SBZs are indicated by the characters of the same colors.

STM images show poor consistency with experimental STM ones.

Figure 3 shows the experimental Fermi maps obtained with ARPES from the SIC-Pb [Fig. 3(a)] and $14\times\sqrt{3}$-Pb [Fig. 3(b)] surfaces. One can see that at a glance the Fermi maps look basically similar. The difference between them resides in the appearance of the features having 1D character in the Fermi map of the $14\times\sqrt{3}$-Pb surface, which features are especially distinctly seen in the first 1×1 SBZ. In order to clarify their origin, we have conducted the DFT calculations, which results on the band structure of the $14\times\sqrt{3}$-Pb surface calculated without and with spin-orbit coupling (SOC) contribution are shown in Figs. 4(a) and 4(b), respectively. One may see the emergence of nine metallic holelike surface bands dispersing in the $\bar{\Gamma}$-$\bar{X}$ direction and having purely one-dimensional character, while in the $\bar{\Gamma}$-$\bar{Y}$ direction only one metallic band disperses, which forms a holelike pocket around the $\bar{\Gamma}$ point. In general, the electronic spectrum has a highly anisotropic character, especially in the vicinity of the Fermi level and demonstrates large Rashba-type spin splitting.

Comparison of the calculated results with the corresponding ARPES spectra for the $14\times\sqrt{3}$-Pb surface, as well as those for the ideal $\sqrt{3}\times\sqrt{3}$-Pb and SIC-Pb surfaces, is illustrated in Fig. 5. In particular, one can see that the dispersions calculated for the ideal $\sqrt{3}\times\sqrt{3}$-Pb surface fit well the dispersions displayed in the ARPES spectrum from the SIC-Pb phase [Fig. 5(a)]. Figure 5(b) shows the ARPES spectrum from the $14\times\sqrt{3}$-Pb surface, where one can notice the appearance of the additional spectral features crossing the Fermi

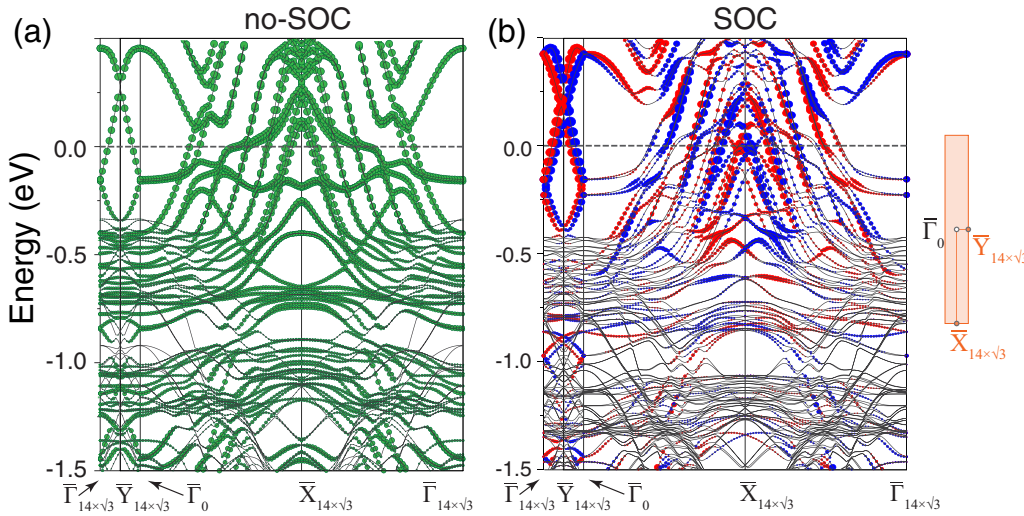

FIG. 4. Calculated electronic band structure of the $14\times\sqrt{3}$-Pb surface (a) without and (b) with SOC included. The size of the green circles in (a) reflects the strength of the surface states. The bands with opposite spin orientation are highlighted in (b) by red and blue circles, which size indicates the degree of spin polarization parallel to the surface. The $14\times\sqrt{3}$ SBZ with high-symmetry points indicated is shown in the right panel.

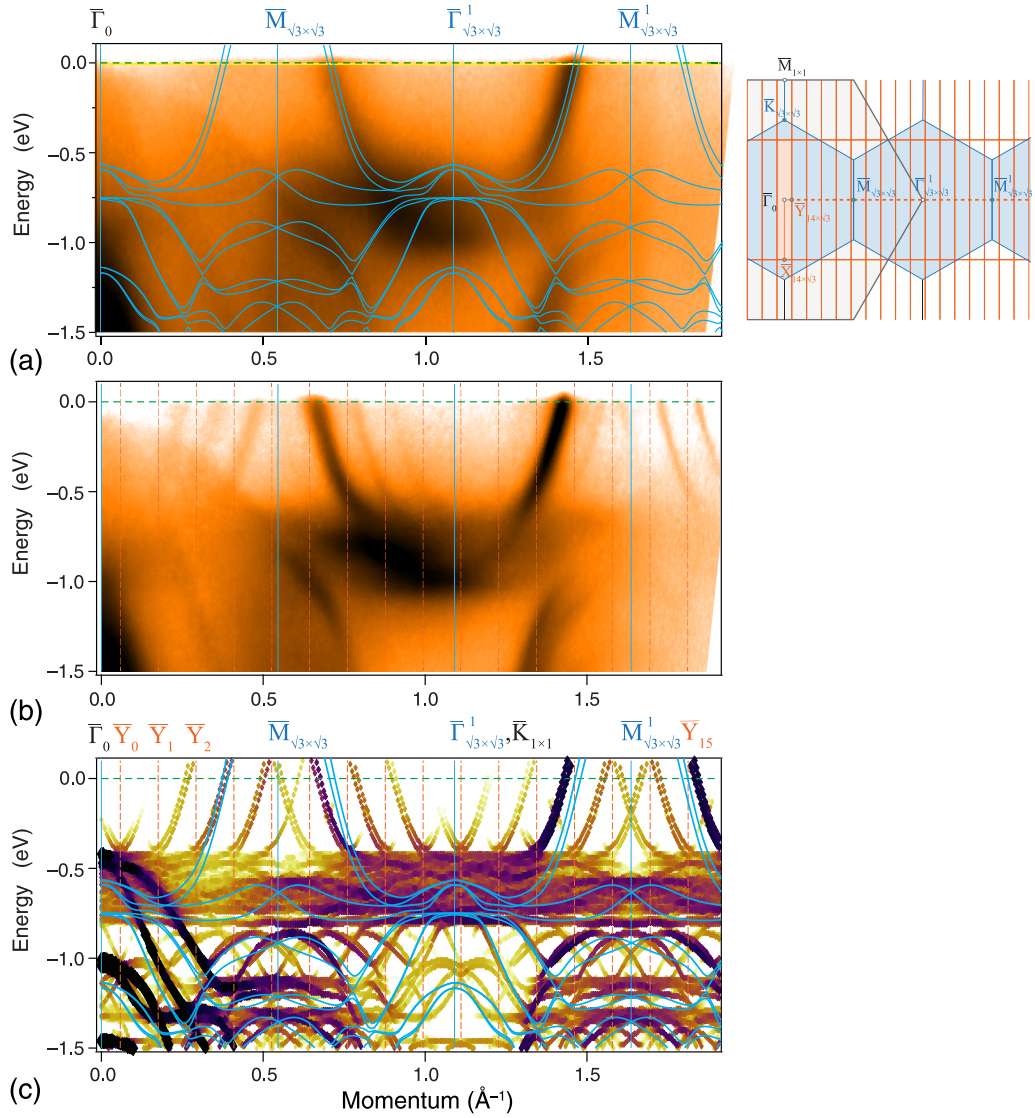

FIG. 5. ARPES spectra from (a) SIC-Pb and (b) $14\times\sqrt{3}$-Pb phases. (c) Calculated electronic band structure of the $14\times\sqrt{3}$-Pb surface unfolded into the 1×1 SBZ. The strength of the states in (c) is indicated using the color pallet where the strength increases in a course from yellow to violet. The calculated dispersions of the ideal $\sqrt{3}\times\sqrt{3}$ surface with 4/3 ML of Pb are displayed in (a) and (c) with the blue lines. Schematic diagram in the right panel illustrates the mutual location of the 1×1 SBZ (hatched in light gray and outlined with black lines), $\sqrt{3}\times\sqrt{3}$ SBZ (hatched in blue and outlined with blue lines), and $14\times\sqrt{3}$ SBZ (hatched in light orange and outlined with orange lines). The pass along which the ARPES spectra were recorded is indicated by the dashed orange line.

level. In order to compare these ARPES data with the results of the DFT calculations, the calculated electronic band structure for the $14\times\sqrt{3}$-Pb surface was unfolded into the 1×1 SBZ [Fig. 5(c)]. From comparison, one can clearly see that each of the spectral features seen in the ARPES spectrum is exactly reproduced in the calculated unfolded spectrum with remarkably high accuracy, which serves an additional argument in favor of the structural model proposed for the $14\times\sqrt{3}$-Pb phase [Fig. 2(a)].

As mentioned above, the procedure for the preparation of the $14\times\sqrt{3}$-Pb surface might be a useful tool to scan the narrow Pb coverage range from 1.20 ML to 1.29 ML in a step-by-step manner using sequential deposition of the desired amount of Pb at each step. We employed this approach in studying the evolution of the transport (superconducting) properties of the Pb/Si(111) system with the growing Pb coverage in this range. It is worth noting that we encountered two difficulties in this study. First, the Pb coverage interval of less than 0.1 ML is so narrow that it is difficult to sustain the deposited Pb doses with a desired accuracy, which hampers accurate evaluation of the resultant Pb coverage. However, monotonic growth of Pb coverage within a particular experimental series was apparently guaranteed. The second obstacle is associated with the drawback of our cooling system with the minimal accessible temperature of ∼2.0 K. The critical temperatures of the samples under investigation appeared to be below this value; hence we were unable to observe resistance drop to zero. Thus, in order to evaluate the critical temperature, we employed fitting of the experimental dependencies to the Aslamazov-Larkin-Maki-Thompson

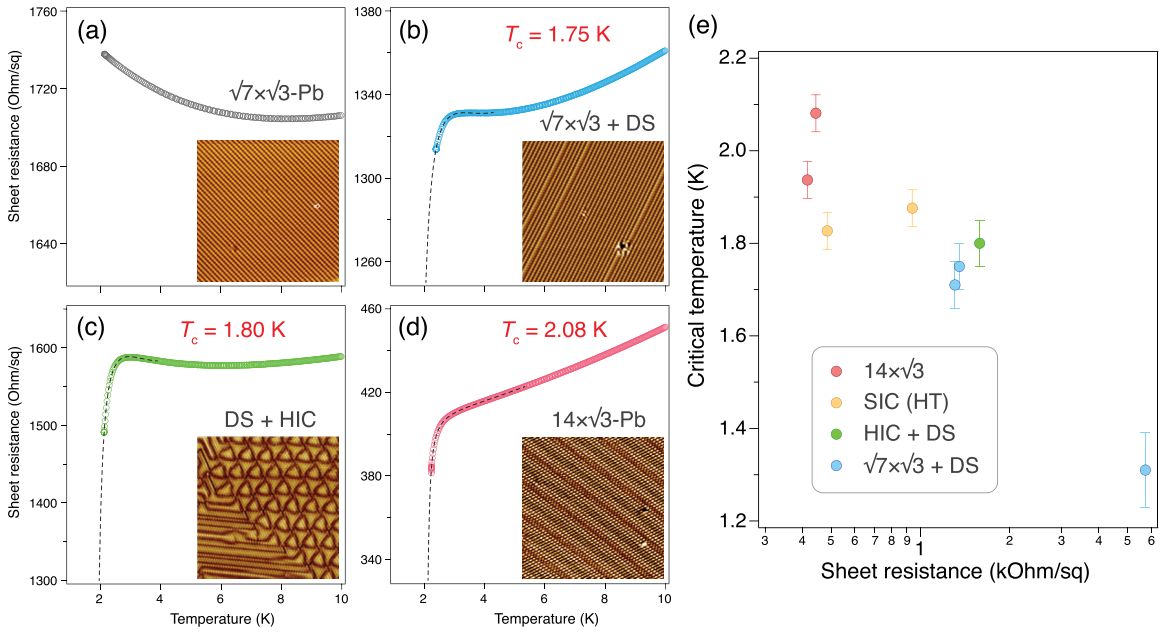

FIG. 6. Temperature dependence of the sheet resistance for the (a) $\sqrt{7}\times\sqrt{3}$-Pb phase, (b) coexisting $\sqrt{7}\times\sqrt{3}$-Pb and "devil's staircase" (DS) phases, (c) coexisting DS-Pb and HIC-Pb phases, and (d) $14\times\sqrt{3}$-Pb phase. The ALMT fits are shown by dashed black curves superposed on the experimental dependencies. The surface structure of the corresponding samples is shown in the insets. (e) Summarizing graph tying together the critical temperature T_c and the sample sheet resistance. The corresponding sample structures are indicated by the color of the experimental dots according to the legend in the inner panel.

(ALMT) corrections [38–40] accounting for the addition to the conductivity above the transition from the fluctuating Cooper pairs supplemented with the temperature dependence of the normal phase resistance $R_0(T)$. Since it is an indirect method to evaluate T_c, we tried to estimate accuracy of the evaluation. The typical random error associated with fitting of the experimental data to the ALMT corrections appeared as small as ±0.005 K. Using available examples with systems where resistance drops to zero at temperatures accessible in our setup (e.g., (Tl, Pb)/Si(111) with $T_c = 2.4$ K [41], (Pb, Au)/Si(100) with $T_c = 2.70$ K [42], and rect-$\sqrt{7}\times\sqrt{3}$-In on Si(111) with $T_c = 2.91$ K [43]), we compared the T_c obtained with the ALMT fitting and that measured at the $R(T)$ dependence drop when it reaches half of the R_0. Discrepancy of the values did not exceed ∼0.08 K.

Figures 6(a)–6(d) present a set of $R(T)$ dependencies measured on the Pb/Si(111) sample with increasing Pb coverage within the same series. The insets illustrate the surface structure of the sample at each stage. One can see that the $\sqrt{7}\times\sqrt{3}$-Pb sample [Fig. 6(a)] has the maximal resistance which increases with lowering temperatures plausibly due quantum corrections and there are no indications on the superconductivity, at least in the given temperature range. However, with the onset of the appearance of the DS-Pb inclusions, the sample starts to exhibit the superconducting properties [Fig. 6(b)], which enhance with growing Pb coverage. The critical temperature gradually increases from 1.75 K for the ($\sqrt{7}\times\sqrt{3}$ + DS)-Pb sample [Fig. 6(b)] via 1.80 K for the (DS+HIC)-Pb sample [Fig. 6(c)] to 2.08 K for the $14\times\sqrt{3}$-Pb sample [Fig. 6(d)].

Figure 6(e) summarizes the obtained data tying together the critical temperature T_c and the sample sheet resistance. The data taken from Figs. 6(a)–6(d) are supplemented by the data from the other series, as well as by the results on the SIC-Pb samples obtained upon conventional high-temperature Pb growth. One can see that, in general, the lower the resistance, the higher the critical temperature. The critical temperature monotonically grows with Pb coverage, though the dependence of resistance is not so straightforward [e.g., the (DS+HIC)-Pb sample has resistance somewhat higher than that of some ($\sqrt{7}\times\sqrt{3}$ + DS)-Pb samples]. One can also notice that critical temperatures determined for the $14\times\sqrt{3}$-Pb samples are systematically higher than those for the SIC-Pb samples.

IV. DISCUSSION

The $14\times\sqrt{3}$-Pb phase has been found to adopt 1.286 ML of Pb. It is of interest to compare it with the ideal $\sqrt{3}\times\sqrt{3}$-Pb structure as well, as with the conventional SIC-Pb phase. The genetic relation of the $14\times\sqrt{3}$-Pb phase to the ideal $\sqrt{3}\times\sqrt{3}$-Pb structure with 4/3 ML of Pb is illustrated in Fig. 7(a). As a starting unit cell, the $9\sqrt{3}\times\sqrt{3}$ one [outlined with the blue parallelogram in Fig. 7(a)] is taken, which is essentially a $\sqrt{3}\times\sqrt{3}$ unit cell nine times extended in the one $\sqrt{3}$ direction. According to the ideal $\sqrt{3}\times\sqrt{3}$-Pb structure, the $9\sqrt{3}\times\sqrt{3}$ unit cell (which area equals 27 1×1 unit cells) incorporates 36 Pb atoms. The $\sqrt{189}\times\sqrt{3}$ unit cell (hatched in yellow and outlined by the red parallelogram) is equivalent to the $9\sqrt{3}\times\sqrt{3}$ unit cell. In order to adjust the unit cell in a way that it would adopt a periodicity along the main 1×1 crystallographic direction, the $\sqrt{189}\times\sqrt{3}$ unit cell is rotated by 3.54° toward this direction and expanded by ∼3.57% along this direction, thus becoming the $14\times\sqrt{3}$ unit cell (hatched in

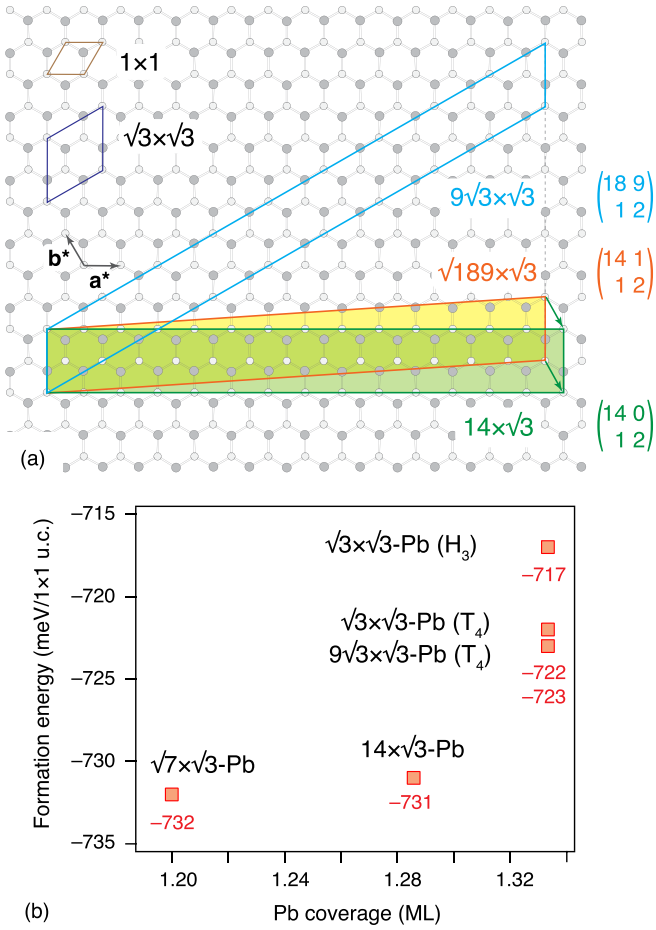

FIG. 7. (a) Schematic diagram illustrating the relation of the $14\times\sqrt{3}$-Pb phase to the ideal $\sqrt{3}\times\sqrt{3}$-Pb phase with transition from the $9\sqrt{3}\times\sqrt{3}$ unit cell (outlined with blue parallelogram) via $\sqrt{189}\times\sqrt{3}$ unit cell (hatched in yellow and outlined by the red parallelogram) to the $14\times\sqrt{3}$ unit cell (hatched in light green and outlined by the green rectangle). The 1×1 and $\sqrt{3}\times\sqrt{3}$ unit cells are outlined by the brown and black rhombuses, respectively. (b) Calculated formation energies normalized to the 1×1 unit cell for the $\sqrt{7}\times\sqrt{3}$-Pb, $14\times\sqrt{3}$-Pb, and ideal $\sqrt{3}\times\sqrt{3}$-Pb phases with various Pb regular sites, H_3 and T_4, as well as with the extended $9\sqrt{3}\times\sqrt{3}$ unit cell. Alternative structural models, namely the $14\times\sqrt{3}$-Pb structure built according to the "devil's staircase" model with six $\sqrt{3}\times\sqrt{3}$ unit cells separated by two $\sqrt{7}\times\sqrt{3}$ units [17] and $13\times\sqrt{3}$-Pb structure [2], appears to be strongly energetically unfavorable, characterized by formation energies of −704 meV and −694 meV, respectively.

light green and outlined by the green rectangle). Due to the expansion, its area becomes 28 1×1 unit cells and incorporating the same 36 Pb atoms it adopts 1.286 ML of Pb. Our STM observations confirmed the results of Ref. [17] that the $14\times\sqrt{3}$-Pb phase is the highest-coverage phase, as further dosing of the $14\times\sqrt{3}$-Pb phase with Pb leads to the formation of the 3D Pb islands on it.

According to the results of the DFT calculations [Fig. 7(b)], the $14\times\sqrt{3}$-Pb phase has formation energy slightly higher than that of the $\sqrt{7}\times\sqrt{3}$-Pb phase, but noticeably lower than the formation energies calculated for the ideal $\sqrt{3}\times\sqrt{3}$-Pb phases with various Pb regular sites, H_3 and T_4, as well as with the extended $9\sqrt{3}\times\sqrt{3}$ unit cell, which can be treated as an additional argument for the $14\times\sqrt{3}$-Pb phase being the highest-coverage Pb/Si(111) phase, which can be realized in the experiment. The other possible competitor is the SIC-Pb phase, which Pb coverage is estimated to be in the 1.28–1.30 ML range [2,20] and its structure is treated as built of the domains with local $\sqrt{3}\times\sqrt{3}$-Pb structure and meandering quasi-$\sqrt{7}\times\sqrt{3}$-Pb boundaries. The alternative viewpoint is that the SIC-Pb phase can be treated as a polycrystal form of the single-crystal $14\times\sqrt{3}$-Pb phase. However, an accurate structural assessment of the SIC-Pb phase is hampered by the lacking long-range ordering in its structure. Moreover, the SIC-Pb phase seems not to be a definite phase with the well-defined structure, but rather a set of structures, which Pb contents, domain size, density, and types of the defects depend on the preparation conditions. In particular, this variation is reflected in the variance of the transport properties of the SIC-Pb phase, normal phase sheet resistance (variation from ∼350–500 ohms [19,23] to 1200 ohms [9,19]; see also Fig. S3 of the Supplemental Material [44]), and critical temperature (variation from ∼1.1–1.2 [9,19,23] to 1.51 K [19] and ∼1.8–1.9 K, as in the present work).

Results of the present transport measurements, especially when being compared with the reported data, demonstrate that the superconducting properties of the single-atom Pb layers are highly sensitive to their real structure obtained in the given experiment and also dependent on the analytical technique, which overall leads to the variation of the results. As mentioned above, the $T_c \sim 1.8$–1.9 K determined in the present study for the SIC-Pb phase well exceeds the other values obtained in the previous transport measurements [9,19,23], but it coincides with $T_c = 1.83$ K obtained in the STS measurements [8]. The still greater $T_c = 2.08$ K for the $14\times\sqrt{3}$-Pb phase can be reasonably attributed to its advanced structural ordering. On the other hand, our transport measurements on the pristine $\sqrt{7}\times\sqrt{3}$-Pb phase did not reveal an indication on the occurrence of superconducting properties (at least, down to ∼2 K) [Fig. 6(a)], while the STS measurements yielded $T_c = 1.52$ K [8]. The intriguing observation within our transport measurements is that the samples with seemingly tiny inclusions of the DS-Pb stripes within the $\sqrt{7}\times\sqrt{3}$-Pb arrays start to display the superconducting properties [see Figs. 6(b) and 6(e)]. Exploring the outbreak of the superconductivity in the single-atom Pb layers on Si(111) can be an interesting and challenging task, but it requires the extremely precise control of the Pb coverage and ability to access to the very low temperatures (well below ∼2 K, accessible in our experimental setup).

V. CONCLUSIONS

In conclusion, we have found that the two-step procedure, where at the first step the Si(111)$\sqrt{7}\times\sqrt{3}$-Pb surface (displaying the 1×1 structure at RT) is prepared using RT deposition of Pb onto Si(111)7×7 followed by annealing, while at the second step, an additional Pb is deposited at RT sequentially until the Pb-densest $14\times\sqrt{3}$-Pb phase with 1.286 ML of Pb covers the entire surface. The single-domain orientation of the $14\times\sqrt{3}$-Pb layer is set along the direction perpendicular to the $[1\bar{1}0]$ atomic steps of the Si(111) substrates and it is preserved

along the entire surface of the terraces which are typically as wide as dozens of nanometers and in the selected areas might exceed a hundred nanometers. The $14\times\sqrt{3}$-Pb phase hosts the superconductivity with the critical temperature $T_c = 2.08$ K which exceeds all ever reported values for the single-atom Pb layers on Si(111).

As a final remark, we have to admit that the reasons for the increased critical temperature of the $14\times\sqrt{3}$-Pb phase are not clearly disclosed. Simple explanations can be based on the association with the increased atomic Pb density within the $14\times\sqrt{3}$-Pb layer or its improved structural quality. However, the reasons might not be so simple and apparent. More serious theoretical considerations are actually required (in particular, assessment of the electron-phonon coupling strength) to get the better-grounded explanation.

ACKNOWLEDGMENTS

The work was supported by the Russian Science Foundation (Grant No. 19-12-00101) [45]. The calculations were conducted using the equipment of the Shared Resource Center "Far Eastern Computing Resource" IACP FEB RAS [46].

[1] X. Y. Ren, H. J. Kim, S. Yi, Y. Jia, and J. H. Cho, Spin-orbit coupling effects on the stability of two competing structures in Pb/Si(111) and Pb/Ge(111), Phys. Rev. B **94**, 075436 (2016).

[2] C. Brand, S. Muff, M. Fanciulli, H. Pfnür, M. C. Tringides, J. H. Dil, and C. Tegenkamp, Spin-resolved band structure of a densely packed Pb monolayer on Si(111), Phys. Rev. B **96**, 035432 (2017).

[3] M. Yakes, M. Hupalo, M. A. Zaluska-Kotur, Z. W. Gortel, and M. C. Tringides, Low-Temperature Ultrafast Mobility in Systems with Long-Range Repulsive Interactions: Pb/Si(111), Phys. Rev. Lett. **98**, 135504 (2007).

[4] M. Hupalo and M. C. Tringides, Ultrafast kinetics in Pb/Si(111) from the collective spreading of the wetting layer, Phys. Rev. B **75**, 235443 (2007).

[5] K. L. Man, M. C. Tringides, M. M. T. Loy, and M. S. Altman, Anomalous Mass Transport in the Pb Wetting Layer on the Si(111) Surface, Phys. Rev. Lett. **101**, 226102 (2008).

[6] A. V. Matetskiy, L. V. Bondarenko, D. V. Gruznev, A. V. Zotov, A. A. Saranin, and M. C. Tringides, Structural transformations in Pb/Si(111) phases induced by C_{60} adsorption, J. Phys.: Condens. Matter **25**, 395006 (2013).

[7] E. Granato, S. C. Ying, K. R. Elder, and T. Ala-Nissila, Anomalous Fast Dynamics of Adsorbate Overlayers near an Incommensurate Structural Transition, Phys. Rev. Lett. **111**, 126102 (2013).

[8] T. Zhang, P. Cheng, W. J. Li, Y. J. Sun, G. Wang, X. G. Zhu, K. He, L. Wang, X. Ma, X. Chen, Y. Wang, Y. Liu, H. Q. Lin, J. F. Jia, and Q. K. Xue, Superconductivity in one-atomic-layer metal films grown on Si(111), Nat. Phys. **6**, 104 (2010).

[9] M. Yamada, T. Hirahara, and S. Hasegawa, Magnetoresistance Measurements of a Superconducting Surface State of In-Induced and Pb-Induced Structures on Si(111), Phys. Rev. Lett. **110**, 237001 (2013).

[10] S. Stepanovsky, M. Yakes, V. Yeh, M. Hupalo, and M. C. Tringides, The dense α-$\sqrt{3}\times\sqrt{3}$Pb/Si(111) phase: A comprehensive STM and SPA-LEED study of ordering, phase transitions and interactions, Surf. Sci. **600**, 1417 (2006).

[11] C. Kumpf, M. Nielsen, R. Feidenhans'l, Y. Su, and R. L. Johnson, Covalent-bond stabilization of the Si(111)-$(3, 2)\times(-1, 1)$-Pb structure, Surf. Sci. **486**, L495 (2001).

[12] S. Brochard, E. Artacho, O. Custance, I. Brihuega, A. M. Baró, J. M. Soler, and J. M. Gómez-Rodríguez, *Ab initio* calculations and scanning tunneling microscopy experiments of the Si(111)-$(\sqrt{7}\times\sqrt{3})$-Pb surface, Phys. Rev. B **66**, 205403 (2002).

[13] C. H. Hsu, F. C. Chuang, M. A. Albao, and V. Yeh, Electronic structure of the Pb/Si(111)-$(\sqrt{7}\times\sqrt{3})$ surface reconstruction: A first-principles study, Phys. Rev. B **81**, 033407 (2010).

[14] S. C. Jung and M. H. Kang, Triple-domain effects on the electronic structure of Pb/Si(111)-$(\sqrt{7}\times\sqrt{3})$: Density-functional calculations, Surf. Sci. **605**, 551 (2011).

[15] M. Hupalo, T. L. Chan, C. Z. Wang, K. M. Ho, and M. C. Tringides, Atomic models, domain-wall arrangement, and electronic structure of the dense Pb/Si(111)-$\sqrt{3}\times\sqrt{3}$ phase, Phys. Rev. B **66**, 161410(R) (2002).

[16] M. Hupalo, J. Schmalian, and M. C. Tringides, "Devil's Staircase" in Pb/Si(111) Ordered Phases, Phys. Rev. Lett. **90**, 216106 (2003).

[17] W. H. Choi, H. Koh, E. Rotenberg, and H. W. Yeom, Electronic structure of dense Pb overlayers on Si(111) investigated using angle-resolved photoemission, Phys. Rev. B **75**, 075329 (2007).

[18] A. Petkova, J. Wollschläger, H. L. Günter, and M. Henzler, Formation and commensurate analysis of "incommensurate" superstructures of Pb on Si(111), Surf. Sci. **471**, 11 (2001).

[19] Y. Sato, M. Haze, R. Nemoto, W. Qian, S. Yoshizawa, T. Uchihashi, and Y. Hasegawa, Squeezed Abrikosov-Josephson Vortex in Atomic-Layer Pb Superconductors Formed on Vicinal Si(111) Substrates, Phys. Rev. Lett. **130**, 106002 (2023).

[20] C. Brun, T. Cren, V. Cherkez, F. Debontridder, S. Pons, D. Fokin, M. C. Tringides, S. Bozhko, L. B. Ioffe, B. L. Altshuler, and D. Roditchev, Remarkable effects of disorder on superconductivity of single atomic layers of lead on silicon, Nat. Phys. **10**, 444 (2014).

[21] H. Kim, S. Z. Lin, M. J. Graf, Y. Miyata, Y. Nagai, T. Kato, and Y. Hasegawa, Electrical Conductivity through a Single Atomic Step Measured with the Proximity-Induced Superconducting Pair Correlation, Phys. Rev. Lett. **117**, 116802 (2016).

[22] F. Oguro, Y. Sato, K. Asakawa, M. Haze, and Y. Hasegawa, Enhanced critical magnetic field for monoatomic-layer superconductor by Josephson junction steps, Phys. Rev. B **103**, 085416 (2021).

[23] D. S. Baranov, S. Vlaic, J. Baptista, E. Cofler, V. S. Stolyarov, D. Roditchev, and S. Pons, Gold atoms promote macroscopic superconductivity in an atomic monolayer of Pb on Si(111), Nano Lett. **22**, 652 (2022).

[24] J. Noffsinger and M. L. Cohen, Superconductivity in monolayer Pb on Si(111) from first principles, Solid State Commun. **151**, 421 (2011).

[25] I. Y. Sklyadneva, R. Heid, K. P. Bohnen, P. M. Echenique, and E. V. Chulkov, Electron-phonon coupling and superconductivity in the (4/3)-monolayer of Pb on Si(111): Role of spin-orbit interaction, Phys. Rev. B **97**, 195409 (2018).

[26] W. Zhao, Q. Wang, M. Liu, W. Zhang, Y. Wang, M. Chen, Y. Guo, K. He, X. Chen, Y. Wang, J. Wang, X. Xie, Q. Niu, L. Wang, X. Ma, J. K. Jain *et al.*, Evidence for Berezinskii-Kosterlitz-Thouless transition in atomically flat two-dimensional Pb superconducting films, Solid State Commun. **165**, 59 (2013).

[27] K. S. Kim and H. W. Yeom, Radial Band Structure of Electrons in Liquid Metals, Phys. Rev. Lett. **107**, 136402 (2011).

[28] S. C. Jung and M. H. Kang, Dynamical nature of the high-temperature Pb/Si(111)-1×1 phase, Phys. Rev. B **84**, 155422 (2011).

[29] G. Kresse and J. Hafner, *Ab initio* molecular dynamics for liquid metals, Phys. Rev. B **47**, 558 (1993).

[30] G. Kresse and D. Joubert, From ultrasoft pseudopotentials to the projector augmented-wave method, Phys. Rev. B **59**, 1758 (1999).

[31] P. E. Blöchl, Projector augmented-wave method, Phys. Rev. B **50**, 17953 (1994).

[32] J. P. Perdew, K. Burke, and M. Ernzerhof, Generalized Gradient Approximation Made Simple, Phys. Rev. Lett. **77**, 3865 (1996).

[33] P. V. C. Medeiros, S. Stafström, and J. Björk, Effects of extrinsic and intrinsic perturbations on the electronic structure of graphene: Retaining an effective primitive cell band structure by band unfolding, Phys. Rev. B **89**, 041407(R) (2014).

[34] P. V. C. Medeiros, S. S. Tsirkin, S. Stafström, and J. Björk, Unfolding spinor wave functions and expectation values of general operators: Introducing the unfolding-density operator, Phys. Rev. B **91**, 041116(R) (2015).

[35] E. Ganz, I. S. Hwang, F. Xiong, S. K. Theiss, and J. A. Golovchenko, Growth and morphology of Pb on Si(111), Surf. Sci. **257**, 259 (1991).

[36] J. M. Gómez-Rodríguez, J. Y. Veuillen, and R. C. Cinti, Scanning tunneling microscopy study of the Si(111)-($\sqrt{3}\times\sqrt{3}$)-Pb mosaic phase, Surf. Sci. **377-379**, 45 (1997).

[37] T. C. Chang, K. Chatterjee, S. H. Chang, Y. H. Lee, and I. S. Hwang, Nucleation and growth of Si on Pb monolayer covered Si(111) surfaces, Surf. Sci. **605**, 1249 (2011).

[38] L. G. Aslamazov and A. I. Larkin, Effect of fluctuations on the properties of a superconductor above the critical temperature, in *30 Years of the Landau Institute – Selected Papers*, edited by I. M. Khalatnikov and V. P. Mineev (World Scientific, Singapore, 1996), pp. 23–28.

[39] F. Sharifi, A. V. Herzog, and R. C. Dynes, Crossover from Two to One Dimension in *in situ* Grown Wires of Pb, Phys. Rev. Lett. **71**, 428 (1993).

[40] A. Larkin and A. Varlamov, *Theory of Fluctuations in Superconductors*, International Series of Monographs on Physics (Oxford University Press, New York, 2005).

[41] A. V. Matetskiy, S. Ichinokura, L. V. Bondarenko, A. Y. Tupchaya, D. V. Gruznev, A. V. Zotov, A. A. Saranin, R. Hobara, A. Takayama, and S. Hasegawa, Two-Dimensional Superconductor with a Giant Rashba Effect: One-Atom-Layer Tl-Pb Compound on Si(111), Phys. Rev. Lett. **115**, 147003 (2015).

[42] L. V. Bondarenko, A. Y. Tupchaya, Y. E. Vekovshinin, D. V. Gruznev, V. G. Kotlyar, T. V. Utas, A. N. Mihalyuk, A. V. Matetskiy, N. V. Denisov, A. V. Zotov, and A. A. Saranin, Gold interlayer promotes superconductivity in single and double atomic Pb layers on Si(100), J. Phys. Chem. Lett. **13**, 10479 (2022).

[43] L. V. Bondarenko, A. Y. Tupchaya, Y. E. Vekovshinin, D. V. Gruznev, A. N. Mihalyuk, N. V. Denisov, A. V. Matetskiy, A. V. Zotov, and A. A. Saranin, Single and double in atomic layers grown on top of a single atomic $NiSi_2$ layer on Si(111), Phys. Rev. B **106**, 035415 (2022).

[44] See Supplemental Material at http://link.aps.org/supplemental/10.1103/PhysRevB.108.115428 for large-scale STM images of the Si(111)14 × $\sqrt{3}$-Pb surface, STM-based structural analysis of the 14 × $\sqrt{3}$-Pb phase and transport measurements on the SIC-Pb samples.

[45] See https://rscf.ru/en/project/19-12-00101/.

[46] See https://cc.dvo.ru.